Materials & Design 210 (2021) 110036

Contents lists available at ScienceDirect

Materials & Design

journal homepage: www.elsevier.com/locate/matdes

Mutual comparison of acoustic, pyrometric and thermographic laser powder bed fusion monitoring

Kai Gutknecht [a,*], Michael Cloots [a], Ryan Sommerhuber [b], Konrad Wegener [c]

[a] Irpd AG, Lerchenfeldstrasse 3, CH-9014 St. Gallen, Switzerland
[b] XARION Laser Acoustics GmbH, Ghegastrasse 3, AT-1030 Vienna, Austria
[c] Institute of Machine Tools and Manufacturing (IWF), ETH Zürich, CH-8092 Zürich, Switzerland

HIGHLIGHTS

- A microphone, a camera and a pyrometer are compared by synchronous application.
- The microphone exhibits the highest sensitivity but is also the most susceptible.
- Position-independent sensitivity has been demonstrated for the optical sensors.
- Microphone placement and compensation recommendations are given.
- Scan direction dependent shield gas interaction was uncovered by all sensors.

GRAPHICAL ABSTRACT

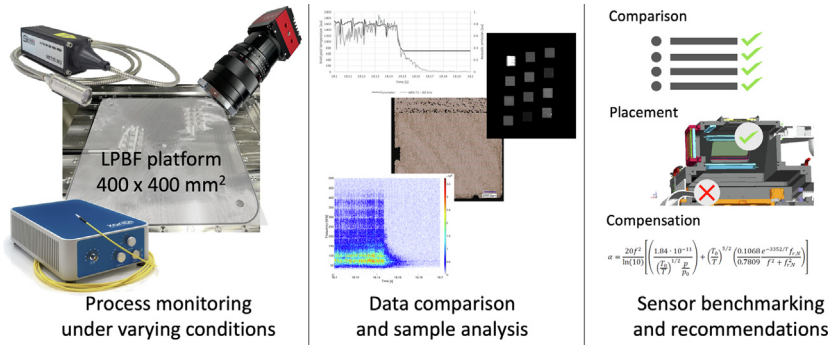

ARTICLE INFO

Article history:
Received 12 April 2021
Revised 19 June 2021
Accepted 7 August 2021
Available online 9 August 2021

Keywords:
Additive manufacturing
Laser powder bed fusion
Airborne noise
Pyrometry
Thermography
Process monitoring

ABSTRACT

This paper compares three distinctive sensors for laser powder bed fusion metal additive manufacturing process monitoring. A microphone for airborne acoustic emissions, an on-axis two-colour pyrometer for melt pool temperature measurement and an off-axis thermographic camera are simultaneously applied. They are challenged with a large build area to investigate their robustness and sensitivity. This paper does not assess the sensors' ability to detect specific process flaws, but instead gives a common ground comparison of general sensor characteristics. The camera provides a descriptive result in form of a heat-map, while it exhibits a lack of sensitivity. In contrast, the microphone presents a sensitivity up to 40 times higher than the camera and is still 15 times more sensitive than the pyrometer. However, with this comes increased susceptibility; its signal strength is strongly dependent on the distance to the melt pool as a result of frequency dependent dissipation. The pyrometer's signal is sensitive enough for relevant process deviations to be uncovered, while being robust towards different sensing distances. Recommendations are given for successful implementation of the sensors. Additionally, novel process phenomena were uncovered: an interaction of the scanning direction with the shielding gas is discussed, plus insights regarding overhang scanning are acquired.

1. Introduction

Laser powder bed fusion (LPBF) is a well-established candidate among metal additive manufacturing (AM) processes. Since its

* Corresponding author.
E-mail address: kai.gutknecht@irpd.ch (K. Gutknecht).

https://doi.org/10.1016/j.matdes.2021.110036

industrialization in the early 2000s, it has seen a constant increase in industry adoption [1]. Process monitoring and control is a key element for improved quality and performance and thus further proliferation of the technology [2,3]. Since recently, most commercially available machines provide some sort of sensor equipment for monitoring the process. However, the calibration and interpretation of the acquired data is usually ceded to the end user, which demands precautions and compromises [4,5]. The most reviewed approaches for sensors applicable in an industrial environment and thus not solely usable in a research facility, are based on optical and acoustical principles [6,7], with the latter not yet available in commercial machines. Photodiodes [5,8–13], pyrometers [14–23], high-speed cameras [5,10,11,16,18,19,24–28], near-infrared (NIR) spectrum thermography cameras [13,17,29–34] and even interferometers [35–37] have been implemented into contemporary LPBF (lab) machines; both into the laser beam path (on-axis) or scanner independent (off-axis). Acoustic sensors either rely on process emissions or require separate stimuli. They are attached to the build plate for structure-bound noise (SBN) detection, or are mounted inside the build chamber to collect airborne noise (ABN) [38–50].

Although a vast number of different types of sensors are investigated individually in literature, an overview and direct comparison on a common basis is scarce [51,52]. Furthermore, most articles focus on specific process phenomena, while neglecting some fundamental measuring problems: An ideal sensor setup is able to provide a signal which captures process deviations/phenomena without being influenced by the ever-changing measuring conditions which are characteristic for the LPBF process. This is mostly disregarded in the aforementioned literature due to the fact that the applied lab machines and conditions do not resemble an industrial size build envelope or industrial process conditions, and thus intrinsically exhibit a more controlled and stable environment. Examples of such **changing measuring conditions** found in industrial machines are related to large build envelopes, complex part geometries and restricted sensor placement. E.g., the signal quality of an on-axis sensor is influenced by the changing measuring distance resulting from the deflection of the beam by the scanner, which is most significant in large build envelopes; another source of deviation is the associated changing angle of incidence on the powder bed and on the scanner mirrors, whose coating performance is typically angle dependent [5,11]. Global sensors such as off-axis cameras and microphones might receive signals from different areas in the build envelope differently, again due to changes in distance, angle and sensing direction. Very little investigation into such topics is presented in the above-mentioned literature, although this needs to be taken into account when assessing process monitoring sensors for modern LPBF machines, which usually have large build envelopes.

The focus of this research is consequently twofold: First, some basic but coherent sensor comparison of the most promising candidates from different domains (optical on- and off-axis as well as acoustic) is provided during the same build job in the same build chamber based on the same events. Second, difficulties in measurement are discussed which are faced upon application of such sensors in an industrial machine with changing measuring conditions. Specific regard is given to the sensors' temporal resolution, sensing distance and scan-direction dependency. Based on this groundwork, an outlook for further improvements regarding sensor selection and integration is given. This paper does not claim to investigate the individual sensors regarding their general ability to detect certain process errors since this is already widely covered in the literature presented above.

2. Experimental setup

This section discusses the machine, the configuration of the build job as well as the sensors' setup and calibration. Additionally, details about the lab methodologies for specimen analysis are provided.

The following experiments have been conducted on a laboratory LPBF system which was all inhouse built. The scope of the machine concept is to provide a robust but still versatile platform for various process related investigations, without compromising the quality of the process and with the overall objective of obtaining results which are transferable to contemporary industrial machines. To this end, it is outfitted with a 400 × 400 mm^2 build plate, a multi-optics option, an open machine control and an uncompromised shielding gas setup. Indeed, the machine concept proves to fulfil industry requirements, since a similar machine is successfully used for commercial additive manufacturing [53]. It is furthermore equipped with three distinctive process monitoring sensors: An on-axis two-colour pyrometer for melt pool monitoring, a microphone with high dynamic range to capture acoustic emissions from the welding process, and a camera aligned off-axis to monitor the thermal emissions of the build process globally.

The machine consists of a 3D scan head with an additional zoom axis integrated for enlarging the beam without the beam waist leaving the working plane of the machine. The nominal beam diameter at the waist is measured as 86 μm ($1/e^2$) and has a beam quality factor of $M^2 < 1.06$, measured according to ISO 11146–1. It can be enlarged up to 180 μm without defocusing. All optical components are thermally stabilized with a water chiller at 22.5 °C ± 0.1 K. The 1 kW IPG YLR type fibre laser in use has a peak wavelength of 1070 nm. The hermetically sealed build chamber is flushed with nitrogen and maintained between 20 and 30 mbar pressure above ambient. The oxygen content throughout the build job is kept below 1500 ppm. Pure nitrogen is used as inert gas. Besides being filtered, the circulated gas is constantly cooled, maintaining a temperature of 23 °C, which also results in a constant machine body temperature. The shielding gas is separated into two streams, one part flushing the laser and monitoring windows at the top of the build chamber, and the other part is used to extract fume and soot from the process. For this purpose, a constant and relatively homogeneous stream across the build plate with a speed of ~ 2.8 m/s is realised and in detail described by Wirth et al. [54]. Stainless steel powder of type 1.4404 (316L) from Carpenter Additive was used. Particle size distribution was characterized as d_{10} = 8 μm, d_{50} = 30 μm and d_{90} = 46 μm by using laser diffractometry.

2.1. Job parameters

This article evolves around one main build job, consisting of two sets of twelve samples each. Their layout on the 400 × 400 mm^2 build plate is depicted in Fig. 1. Sample group 1 is placed in the corner of the build plate, while group 2 is centred under the off-centre placed scanner. The sample identifiers Px.y are composed of a prefix P, the sample type x (1–12) and following the dot the group number y (1 or 2). The scanning order is performed against the shielding gas direction. Accordingly, each layer started with P1 from group 1 (namely P1.1) and ended with P12 from group 2 (P12.2). The dashed line encircled array gives an overview over the ordering of the specimens within those two groups and does not represent a separate group.

The specimens are of cubic shape with edge length of 10 mm. Inverted pyramid supports of 1 mm additional height ensure

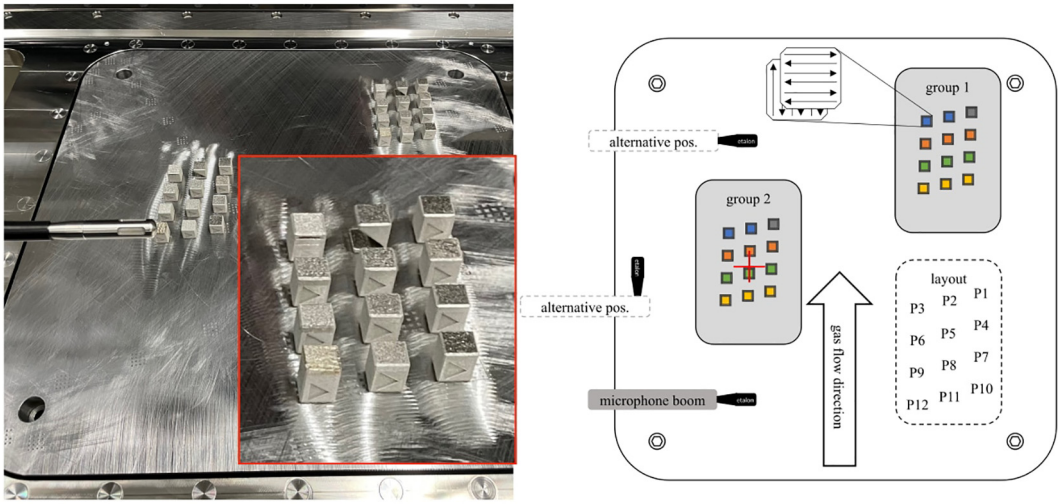

Fig. 1. Left: Build plate after unpacking, with the microphone in the foreground plus a close-up of the specimen group 1. Right: Setting of the build job, consisting of two identical groups of twelve specimens. The center of the scan field is marked with a red cross above P8.2. The microphone's lateral position is depicted, as well as alternative positions for additional investigations. In the upper region, the alternating hatching is schematically depiced by two sets of vectors of two subsequent layers.

simple removal. The first 8.5 mm of all specimens are built using a standard reference parameter set, to ensure a solid carrier. Only the top 2.5 mm of the samples are built using deviating parameters. An exception to this is P12, which involves increased energy input. To not jeopardize other parts, it is stretched in height for parameter alteration only to begin when all other parts are finished. P1 is the reference sample and built without any intentional flaws or deviations from the standard. P2 and P3 are also being entirely built with reference parameters, but embody deviations in geometry, where P2 resembles as wedge shape and P3 contains deliberate voids (details see Section 3.4). The scanning parameters can be retrieved from Table 1. Furthermore, the layer thickness is set at 30 µm for all specimens. All specimens have their number embossed to the side for easier identification.

The parameters were chosen around a proven reference parameter set typically yielding relative densities of above 99.5%. To increase readability of the monitoring data, border scans were omitted, which results in a slight, consistent and thus admissible drop of part density when measured with Archimedes' principle. This reference parameter is applied to specimens 1 through 3, as well as the carriers of all other specimens, as described before. Aside from specimens 1, 2 and 3, three subgroups of specimens were created representing different deviations from those standard parameters: hatch distance, scan speed and volume energy density $e_{V,h}$. The deviation type is also noted in the last column of Table 1. These groups are to provoke process conditions which typically lead to phenomena like increased spatter, lack of fusion, balling etc. while still maintaining a somewhat reliable process condition to not compromise the whole build job. For subgroups 1 and 2, this was mainly achieved by maintaining a constant $e_{V,h}$, which is defined as follows:

$$e_{V,h} = \frac{P}{v \cdot h \cdot t}$$

With P being the laser power, v the scan velocity and h and t denote hatch distance and layer thickness, respectively.

Since the samples are placed in different regions of the build plate, the individual distance from the samples to the microphone, as well as the required inclination of the laser beam, are relevant for the following discussions. The specific values are given in Table 5.

2.2. Microphone

As acoustic sensor, a XARION Eta250 Ultra membrane free microphone is used to record airborne noise (ABN) from the melt pool, transported by the inert atmosphere. This contact-free *optical* microphone utilizes the principle of interferometry to measure sound in a frequency range of 10 Hz to 1 MHz. Any sound passing the microphones etalon in a wave form pressure field changes the local refractive index, which in turn influences the laser beam passing the etalon. Through interferometry, this shift and thus the pressure level representing the sound can be measured. The

Table 1
Specimen properties, # 4–12 apply only for the top part of the specimens, starting at layer 284.

#	Spot diameter $1/e^2$ [mm]	Hatch [mm]	Laser power [W]	Scan speed [mm/s]	Volume energy [J/mm^3]	Variable
1	0.086	0.070	200	1′200	79.4	Reference
2	0.086	0.070	200	1′200	79.4	Geometry (Wedge)
3	0.086	0.070	200	1′200	79.4	Geometry (Voids)
4	0.086	0.030	85	1′200	78.7	Hatch
5	0.086	0.110	315	1′200	79.5	Hatch
6	0.086	0.150	430	1′200	79.6	Hatch
7	0.086	0.070	100	600	79.4	Speed
8	0.086	0.070	400	2′400	79.4	Speed
9	0.086	0.070	800	4′800	79.4	Speed
10	0.12 / 0.15 / 0.18	0.070	200	1′200	79.4	Defocusing
11	0.086	0.070	100	1′200	39.7	Vol energy
12	0.086	0.070	220–360	1′200	87.3–142.9	Vol energy

detailed working principles are thoroughly described by Rohringer et al. [50].

The device's etalon/head is placed inside of the build chamber, taking advantage of a dedicated feed-through for the optical fibre connecting it to the main device. This allows for an airtight sealing of the chamber. The sensor head is protected with a dedicated housing (protection kit) and mounted at the tip of a rod bringing it close to the actual process with enough room vertically (100 mm) for the coater and the shielding gas stream to unimpededly pass by underneath (see Fig. 1 left). The distance in shielding gas direction upstream is 200 mm and 100 mm for groups 1 and 2, respectively. Additionally, group 1 is also 200 mm off to the side (see Fig. 1). Assuming a speed of sound of 350 m/s in pure nitrogen according to Costa Gomes and Trusler [55], those distances result in a delay of 400–900 μs between sound source and microphone. More detailed numbers, which are being used for the signal synchronization, can be retrieved from Table 5. Since the interferometry happens at the speed of light and the rest of the microphone electronics is all analogue, no additional significant signal delay has to be reported. The output signal is recorded using an AC input of a QASS Optimizer4D device. A high-pass 40 kHz filter is applied to cut off any machine-auxiliaries related noise (see also Prieto et al. [42] and Fischer et al. [56]). The signal is sampled with 2 MHz with 24 bit resolution and in parallel, an FFT (31′250 spectras/s, window function Hanning raised cosine) is performed with a frequency resolution of 2 kHz. The resulting amplitude is provided in arbitrary units [au] and wherever possible normalized to obtain handy numbers.

2.3. Pyrometer

The two-colour pyrometer in use is a Sensortherm H322 high-speed pyrometer, based on two InGaAs photodiodes ranging from 1450 to 1800 nm. It has a measuring range of 700–2300 °C with a sampling frequency of 12.5 kHz. Between the scanner's x/y mirrors and the z-axes sits a semi-transparent mirror with which light (400–900 nm and 1300–2100 nm) is extracted from the laser beam path and directed onto the pyrometer's fibre optic (see Fig. 2). Hereby, the pyrometers FOV (field of view) constantly follows the laser-material interaction area. Pre-alignment of the pyrometers FOV, which is between 3 and 4 mm in diameter, to the working laser is performed with their pointer lasers. Fine adjustment is accomplished using a portable temperature source HE1200 also provided by Sensortherm (1200 °C, aperture of ø 0.3 mm) which is placed in the working area of the machine emulating a melt pool. Maximizing the single channel signals from the pyrometer when panning the FOV means, that the heat source is centred in its FOV. The heat source's aperture is beforehand aligned to the pilot laser of the working beam; therefore, the working laser and the pyrometer are concentric. This heat source is also used to calibrate the pyrometer for any given attenuation originating from the scanner optics. It has however to be noted, that this radiation source does not perfectly represent a melt pool, since it differs in material, aggregate state and hence also emissivity. To obtain temperature values on an absolute scale, the emissivity slope would need to be determined, for example by melting the material in question using a melting pot inside the machine. Since this equipment was not available, and for the results of this investigation relative temperature values suffice, a standard value for liquid metal was taken from the pyrometer manual. Therefore, the resulting temperature values are presented as arbitrary units [au], nevertheless the values are similar to °C. The pyrometer outputs its quotient temperature using an analogue current interface, which is set each 80 μs. In order to simplify data synchronization, this output is sampled with a second input on the afore mentioned QASS Optimizer4D with 100 kHz. This guarantees synchronous signal recording as both channels are sampled on the same device.

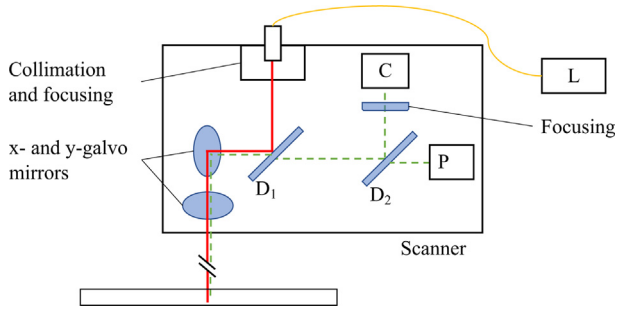

Fig. 2. Optical scheme of the scanner. In solid line depicted is the processing beam, originating from a fibre laser L. The dichroic element D_1 extracts the process signal (dashed line). A second dichroitic mirror D_2 divides it onto a camera C (unused in this study) and a pyrometer's fibre optic P.

2.4. Thermography camera

An off-axis camera is mounted on top and outside of the build chamber next to the scanner, to constitute the thermography system. It is mounted at an angle of 7.5° to the vertical axis to align the centre of the image with the centre of the build plate. The industrial computer vision camera with a resolution of 4096 × 4096 pixels is based on a CMOS-type chip (ON Semi PYTHON 16 K NIR) optimised for increased quantum efficiency in the NIR spectrum (roughly 10% increase compared to a standard chip). Neutral density and bandpass filters ensure that merely light around 850 nm (compromise between chip sensitivity and thermal radiation spectrum [32]) reaches the sensor. The chip temperature of the camera is monitored, assuring that no temperature affected sensitivity shift is happening unnoticed. The temperature increased only by 0.5 K throughout the whole build job, anyway. The acquisition and subsequent image analysis are performed by the machine's programmable logic controller (PLC) in real-time. The camera is triggered in a quasi-long-exposure mode (5 Hz partial image frame rate) at which each partial image undergoes certain noise reduction operations. The final image per layer is adjusted for lens distortion and the skewness of the camera, for all subsequent measurements to be easily transformable into the machine coordinate system. For each layer, a contour detection algorithm extracts the scanned areas and—with the help of the machine coordinates—assigns them the part numbers extracted from the build job file. Average emission and its standard deviation are determined for each such blob (i.e. part) and logged by the PLC. These metrics, aside from the original images of course, are later used for process analysis. The camera's settings are chosen such, that they work for a variety of different materials and process parameter sets without changeover. The image, which covers almost the entirety of the build plate, has an average resolution of 54 μm per pixel. The results of this sensor are referred to as off-axis thermography (OT).

2.5. Lab methodology

Specimens were quantitatively analysed regarding their melt pool size and material density. Solidified melt pool size was measured from the vertically cut specimens. The resulting halves were hot mounted with a Struers CitoPress 5 and afterwards ground and polished (1 μm) on a QATM Saphir 520. The resulting samples were then etched using V2A reagent. Light microscopy was performed on a Keyence VHX-5000 with factor 300 magnification to measure the width and depth of the top layer solidified melt pools (see Gerstgrasser et al. [57] for details on all the methodology). Material density was determined using pore detection on the microscopy

images of the pre-etched samples. Threshold intensity above which a pixel is counted as solid was set to 65%. Furthermore, blobs with a size equivalent to a circle with diameter 10 μm or smaller are disregarded. Verification was done using Archimedes' principle by weighing the samples (before cutting) in air and acetone and comparing the resulting density with the ideal 7.95 g/cm^3 bulk density value [58].

3. Sensor benchmarking

This section serves three goals: first, comparing the sensors regarding their temporal measurement accuracy (Section 3.1); second, discussing overall, location- and direction-dependent sensitivity (Sections 3.2 and 3.3) and third, mutually assessing the sensors' general error detectability on several deliberate process errors (Sections 3.1–3.4).

To that end, the data collected by the three sensors during the above-described build job (roughly 300 gigabytes, of which roughly 85% originate from the microphone and 10% from the pyrometer) is analysed using descriptive statistic approaches to foster the understanding of the underlying measurement principles and their peculiarities. Subsequently, a conclusion is drawn comparing the sensors quantitatively. This work lays the grounds for future more specific defect detectability benchmarking.

3.1. Temporal resolution

Hereinafter, the sensors' temporal resolution is investigated by monitoring an overhang scan and the resulting process anomaly. The geometry of all carrier bodies of the samples built for this article are embossed with their corresponding specimen number to the side of the body, which is then replicated during the build, resulting in a recessed number on the wall of each cube. Wherever there is a horizontal line in that number, there is a potential overhang scenario. This is very prominently the case with the upper horizontal bar of the number '5' of P5. In layer 269, the layers containing this embossed number are surpassed, and thus the cover of the upper bar of the number '5' is scanned, resulting in an overhang situation. This is depicted in Fig. 3 with the resulting OT image on the left, and the scan pattern of layer 268 and 269 (overlayed) on the right. 268 still contains the number, while layer 269 shows a full hatching and thus also holds vectors crossing over the "void" below, where there is only loose powder.

The first five to six vectors of this layer are compromised by this. The overhanging surface has, in contrast to normal hatching, only loose powder underneath, therefore the thermal circumstances are vastly different in that region [13,15]. Furthermore, there is no solid material for the produced melt track to attach to, which in turn is fully exposed to different forces including its residual stresses during the cooling down process. All this leads to increased spatter, as is apparent from the OT image (Fig. 3). Additional effects can be overheating, dimensional inaccuracies etc. [8,13]. Fig. 3 demonstrates, that the OT camera is capable of capturing such a short-lived event, even though the total exposure time of the image taken for this whole layer is 40 s.

In order to demonstrate the temporal resolution of the other two sensors involved, Fig. 4 plots the airborne noise (ABN) and temperature values for one vector affected by the overhang. The depression in the middle of the vector, between 22.0495 and 22.051 s, is clearly visible for the pyrometer, the microphone's readings however are not very indicative.

3.1.1. Temporal resolution of the microphone

Despite the high sampling rate of the microphone, the overhang depicted in Fig. 4 is not noticeable in the recording. Therefore, its temporal resolution is further investigated using a more well-defined incident: the laser-off event. After the last vector of each part, and hence before the execution of the subsequent jump command to the next part, the scanning instructions were complemented with a wait command of 100 ms duration. This simplifies the post-process analysis of the time-based data, as the notable pause enables to distinguish between two parts. Consequently, the laser is already turned off and the scanner does not move any further than the end of the last vector, as skywriting is disabled. This brings the additional benefit of being able to observe—with the pyrometer—any ongoing events after the energy input is halted. The visualization of the respective acoustic data, which is also recorded in parallel, evidently uncovers such a process (see Fig. 5). It comprises the final six vectors of a hatching and the aforementioned wait time in a time–frequency diagram. Frequencies above 250 kHz rapidly die out after the laser is turned off, while there is some sort of reverberation in the lower end of the spectrum, especially notable between 50 and 100 kHz, and persisting for up to 20 ms. This is observable for each instance throughout the experiment.

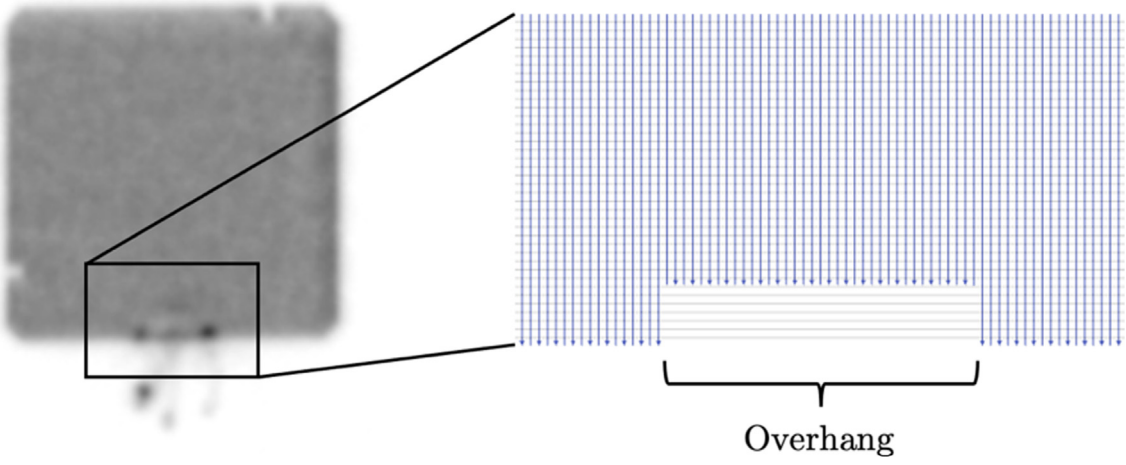

Fig. 3. On the left a small section of the OT image from L269 containing only P5.2. Spatter and overheating in the lower region, where the number '5' is located, are visible as dark blobs (colours are inverted for better legibility). Since this is a small image section of the whole OT image, the resolution is low and thus the image appears blurry. The depicted specimen has an edge length of 10 mm. On the right the scanning pattern overlay of that lower central region of P5.2 is depicted. The blue vertical lines represent L268 and the grey horizontal lines L269.

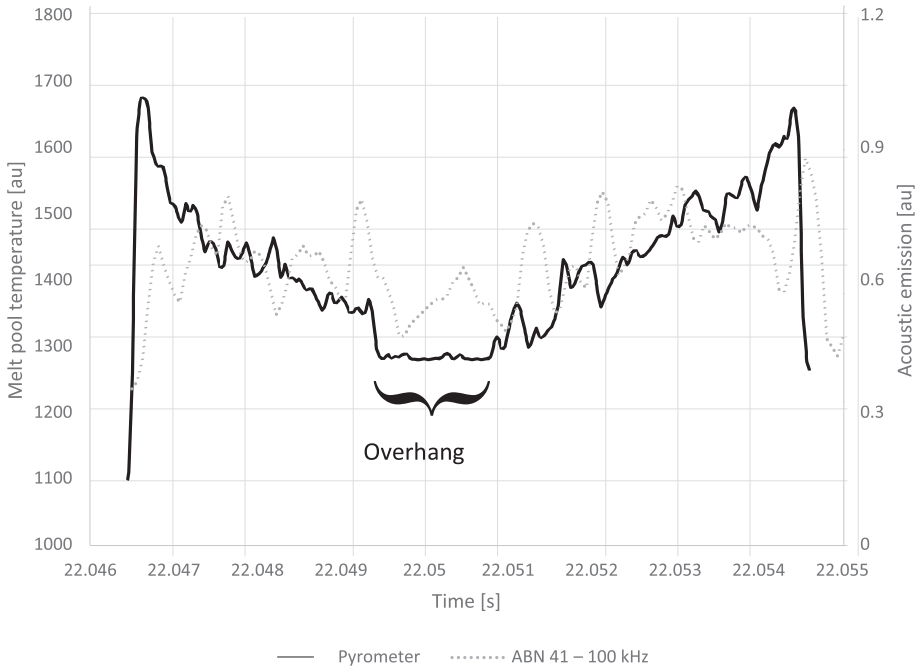

Fig. 4. P5.2, L269, the fourth vector, showing the signal drop for the temperature value in the centre of the chart due to the overhang situation.

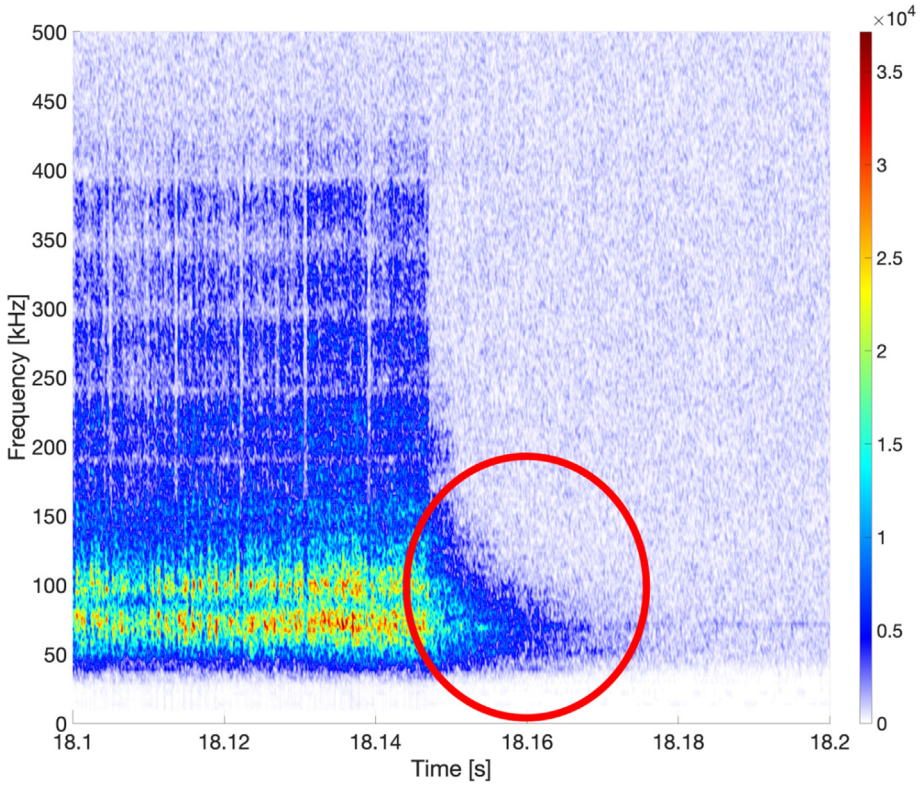

Fig. 5. Dying down of ABN after the scanning of layer 43 (P1.2) has finished. However, reverberation is apparent in the region of 50 – 100 kHz. Frequencies bellow 40 kHz are attenuated by a high-pass filter.

Fig. 6 plots a dedicated frequency band (70–80 kHz) of this residual ABN together with the corresponding temperature values from the pyrometer. Although both data sets are triggered simultaneously, they need to be synchronized post-process by considering their respective delays caused by propagation of sound and digitalization of the pyrometer signal, as presented in Section 2.

The temperature signal exhibits some behaviour similar to a hyperbolic temperature decay, until a value of 700, which is the lower limit of the device, after which it outputs a constant floor value of 700. The acoustic signal mainly follows this behaviour, which raises the question of whether the two measurements are interrelated.

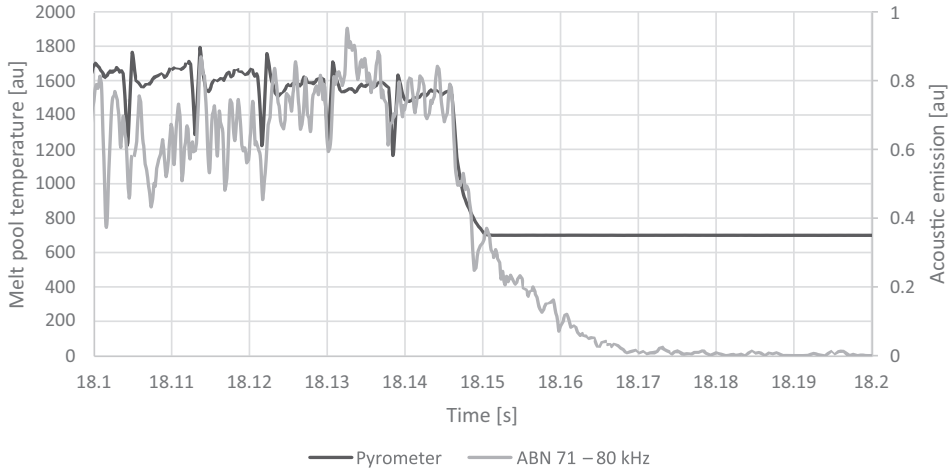

Fig. 6. Plot of temperature and acoustic emission of P1.2 on layer 43 for the final five vectors and some appended delay time. Both signals are smoothed with a central floating mean of 640 μs for better visualization. The arbitrary units of temperature can be interpreted as °C.

The hyperbolic nature of the temperature signal decay can be interpreted as the ongoing cooling process, which in fact can be approximated with the hyperbolic Rosenthal equation. This is a simplified but fundamental model for spot-welding; as explained by Radaj [59] it represents a point source in a half-body, which is comparable with the present conditions at the vector terminus. A rise time and/or propagation delay of the involved electronics can be ruled out as an alternative reason for this decay, based on the following two arguments: The pyrometer's output signal can be set manually for configuration and test purposes. When doing this, a step response is generated on the output electronics. When measuring this response for both rising and falling signals with the given recording system, no overshoot or linear rise time can be detected for the rising case. With a sampling rate of 100 kHz, this means that the signal correctly responses within 10 μs. For the falling step response, four steps are required for the signal to fall from 100% to 0%, resulting in a maximum fall time of 40 μs, which is still below the timescale of the above phenomenon and also faster than the proclaimed 12.5 kHz sampling rate of the pyrometer itself. The second argument then covers the whole signal chain in a qualitative manner: When initiating a jump between two vectors which are far enough apart, such that the vector's (potentially still emitting) terminus leaves the pyrometers FOV, the decay is again faster than what can be observed in Fig. 6. Since the scanner's acceleration and deliberate delays (like mark-delay, laser-off delay etc.) are involved, it is difficult to determine an absolute value, however. Nevertheless, it can be concluded, that in this present case, the pyrometer is in fact measuring the cooling down of the final segment of the vector, without any noticeable impact of the involved electronics' latency.

3.1.2. Reverberation

The source for the matching acoustic signal, which shares the same delay time, can be either originating from the ongoing cooling and solidification process, or be a result of simple reverberation within the build chamber. To investigate reverberation, a theoretical and an experimental path are taken. For the experimental examination, an artificial source of sound is required to generate a strong and extremely short burst—preferably across all frequencies. Such an event, which is ideally like a Dirac delta function equally strong across all frequencies, can be mimicked by breaking a pencil lead [60,61]. This so-called *pencil lead break test* is conducted as follows: A pencil lead of hardness HB and diameter 0.5 mm is extended by 10 mm out of the pencil and broken by pressing its tip against a solid surface to initiate a fracture caused by the bending. An initial test is performed in atmospheric conditions with 16 mm distance to the microphone. The resulting spectrum is depicted in Fig. 7. The ABN overall lasts only for about 0.6 ms and then dies out immediately, with some exceptions in a few frequencies, lasting up to 4 ms. So, in general, the microphone setup shows no sign of reverberation in free atmosphere, as expected.

A second test is performed inside the chamber during a paused build process, to most accurately reflect the process conditions. The process is halted, and the pencil is mounted onto the coater at the powder level. This is done in such a way, that upon moving the coater, the tip of the pencil lead collides with a built part and breaks. The shielding gas stream remains activated for this test. The results are plotted in Fig. 8.

First of all, due to the increased distance to the microphone compared to the primary test, the intensity level is reduced. This is especially the case for the higher frequencies as a result of dissipation. Nevertheless, a reverberation, very similar to what is observed during the process, is detected. Again, most notably around 70–80 kHz, and congruently lasting for about 20 ms. These tests were repeated without the protection kit which encapsulates the etalon. There were no significant differences detected regarding reverberation.

With the reverberation proven experimentally, the theoretical path can be approached for verification. The reverberation time T_{60} is defined as the time it takes for the sound pressure to drop by 60 dB (i.e., by a factor of 1000) after an abrupt ceasing of the source. According to Sabine [62], this time is approximated by the following, empirically developed equation:

$$T_{60} = \frac{24\ln(10)}{c_s} \frac{V}{\sum_i A_i \alpha_i}$$

The volume V and surface area A of the machine are known. The speed of sound c_s in nitrogen around room temperature is given at 350 m/s [55]. The absorption coefficient α_i depends on the material and surface condition of the associated area A_i, as well as the frequency. For the most part of the machine, which consists of aluminium and steel with low surface roughness, this coefficient is assumed to be 0.01, meaning a good reflector. The powder bed and the shielding gas nozzles are approximated to be total absorbers with a coefficient of 1. This results in a reverberation time of 24 ms, which is similar to the experimental results. Unfortunately, available tables provide absorption coefficients to a maxi-

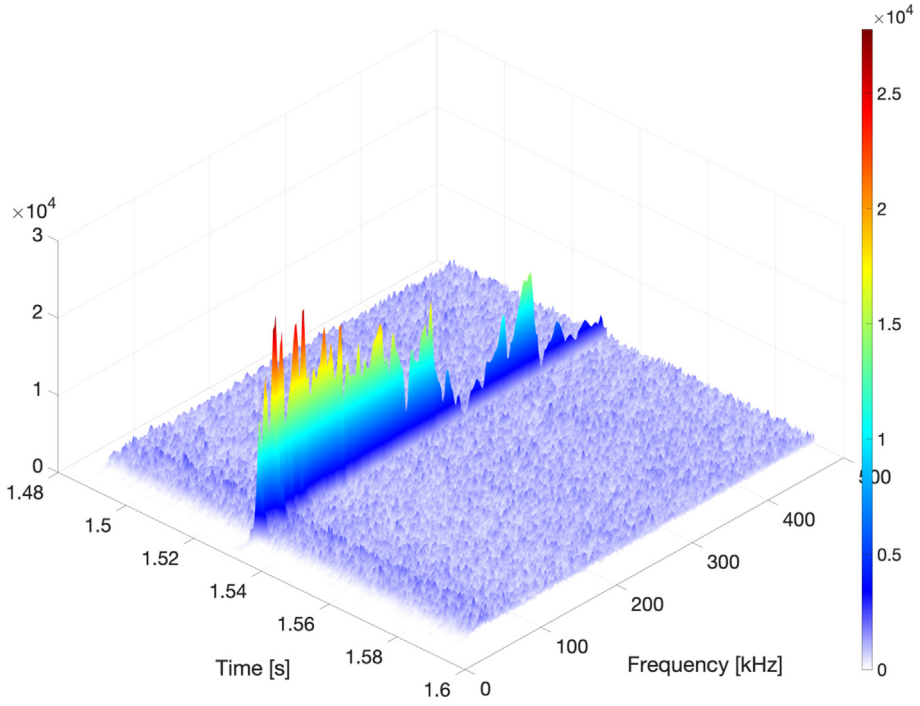

Fig. 7. Pencil lead break test under atmospheric conditions, performed right beside the microphone. The resulting ABN is only 0.6 ms long.

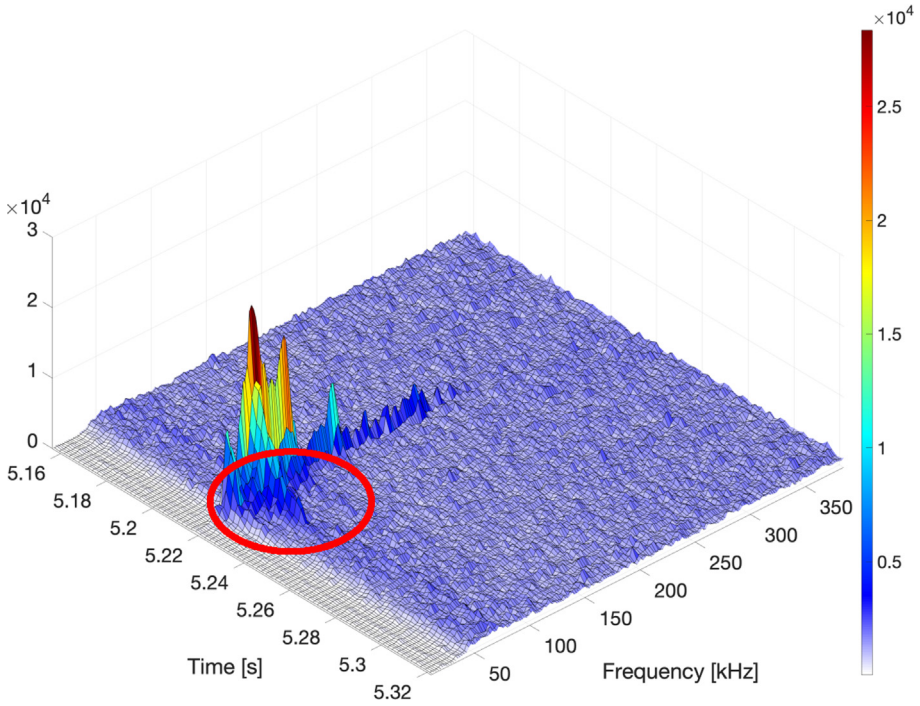

Fig. 8. Pencil lead break test under process conditions inside the build chamber. A relevant reverberation is clearly visible in the expected range below 100 kHz. The resolution is deliberately reduced for visualization purposes.

mum of a few kHz and are thus below the relevant frequency range, therefore, the above assumptions are conservative estimates only.

To conclude, the detected acoustic decay can be attributed to reverberation. This reduces the temporal resolution of the microphone in the frequencies below 100 kHz, since it causes a smearing of the amplitude across time. This is the reason for the signal in Fig. 4 to be almost unaffected by the overhang. This effect therefore needs to be considered in the following analysis.

3.1.3. Results regarding temporal resolution

When plotting the ABN above the reverberation spectrum, as shown in Fig. 9, the microphone's signal is now indicative for the overhang (signal drop below 0.45), but still not as distinctive as

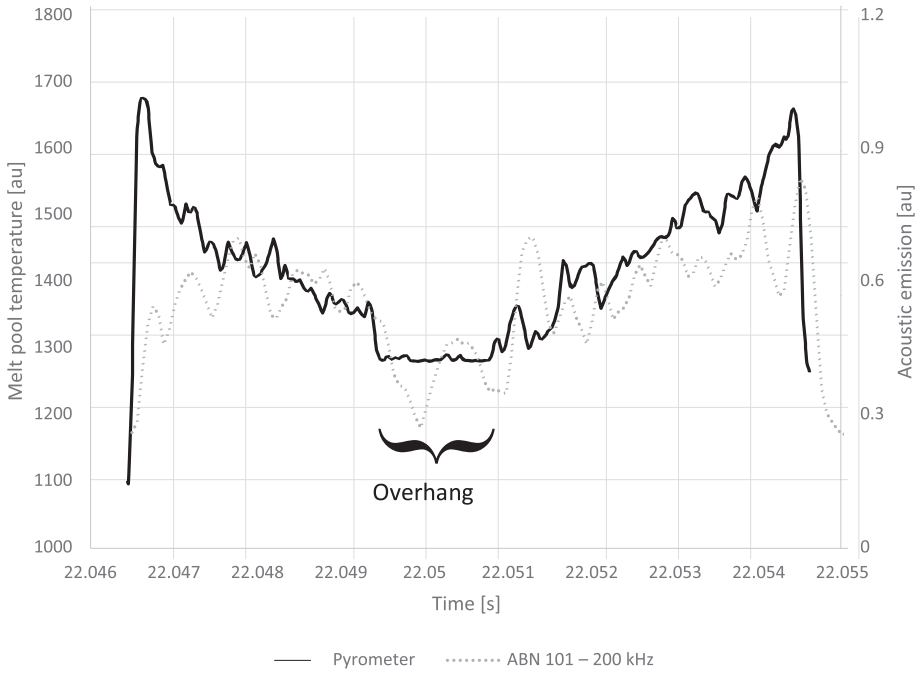

Fig. 9. P5.2, L269, the fourth vector, showing the signal drop for both the temperature value and the ABN (without reverberation) in the centre of the chart due to the overhang.

the pyrometer. The hump in the ABN curve in the middle of the overhang region could be a result of a spatter particle being ejected or landing in the powder bed.

For both, the pyrometer and the microphone, the overhang results in a reduced signal level. This is counter intuitive, since the heat conductivity in loose powder is significantly decreased [13,15]. For the pyrometer, this observation can be reasoned with the argument, that the excessive laser power as a result of the decrease in heat dissipation does not necessarily result in increased temperature, but instead in a larger melt pool and potentially more spatter ejection [8,51,63]. Chivel and Smurov [15] also detected larger melt pool dimensions in overhanging regions and even demonstrated temperature drop for that region with a two-colour pyrometer. A spatially resolving two-colour pyrometer high-speed setup by Hooper [19] yields similar conclusions; compared to conventional vectors, the maximum melt pool temperature is significantly lower for overhang scans (laser power is also lowered, but only marginally). Regarding the microphone, opposite results were found by Plotnikov et al. [52]: They detected increased structure-borne noise (SBN) in unsupported overhanging areas. The details of this discrepancy between ABN and SBN is subject for subsequent studies, however. In this investigation, the encountered decrease for ABN in overhang situations is confirmed by P2 with its wedge shape, where the signal level is similarly decreasing for vectors approaching the overhang.

In conclusion it can be found that all sensors' temporal sensitivity is high enough for recording events happening within a fraction of a vector, where the microphone and pyrometer are deemed superior due to their precise temporal resolution. Since reverberation is present, the analysis of short-lived phenomena is preferably performed above 100 kHz for ABN, although some intrinsic blur still needs to be taken into account. The pyrometer's temporal resolution is reflected by its sampling frequency and can thus be accounted as 80 μs. The microphone without reverberation is equally fast (the actual speed depends on the nature of the effect to be observed and thus the frequency it emphasises), while the resolution of the OT is undetermined but for prominent events certainly in the same order of magnitude.

3.2. Sensing distance and angle

To assess the sensors regarding their susceptibility to the sensing distance and angle as changing measuring conditions, a large build platform and equal process conditions across that platform are required. Fig. 10 provides the signals of all sensors from most of the specimens across the build platform from a layer, where their carrier is being manufactured and thus, they all share the same process parameters and therefore comparable process conditions (except for specimens 2 and 3, hence they are excluded from this analysis).

3.2.1. Non-perpendicular laser beam

The pyrometer's signal and the emission captured by the OT camera perfectly agree. Additionally, for group 1, they exhibit a pattern, which seamlessly maps to the theoretical laser beam roundness (see plot). Due to the extreme deflection in the region of group 1 and the related skewness of the laser beam, the circular Gaussian profile shows some ellipticity in the material-interaction plane. This is expressed as beam diameter aspect ratio in Table 5. The resulting ellipsis covers a larger area, which in turn results in a reduced laser intensity. The observation from Fig. 10 implies a causality between laser intensity and melt pool emissions/temperature. To further investigate this, melt pool dimensions are measured from metallographic images for P1.1 (representing group 1, skewed laser) and P1.2 (group 2, perpendicular laser), Fig. 11 depicts a section of the images used. The results are summarized in Table 2, the methodology is described in Section 2.5. Measurements are taken from the top layer of the specimen, and the first and last ten vectors are neglected. Additional specimens could not be considered, since their last layers were manufactured using different parameter sets, as described in Section 2.1.

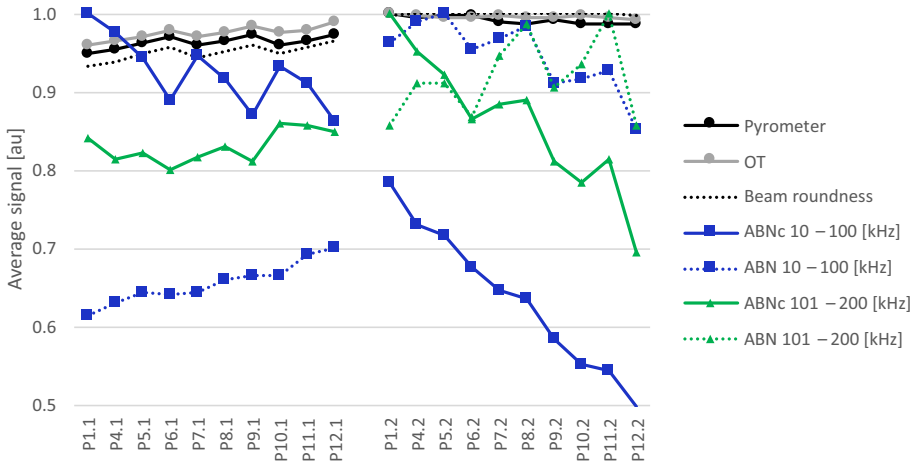

Fig. 10. Average signal of each sensor for each specimen P1.1-P12.2 (excl. P2/3) from layer 41. Each of the six signal-sets is individually normalized to their max. value for better comparison. Beam roundness describes theoretical laser beam ellipticity (ratio of half-axis), where 1 equals a perfect circle (see appendix). The ABN is plotted in two frequency bands. ABN 101 – 200 kHz for group 1 is below 0.5 and thus not visible. ABNc is compensated for dissipation (described in the following).

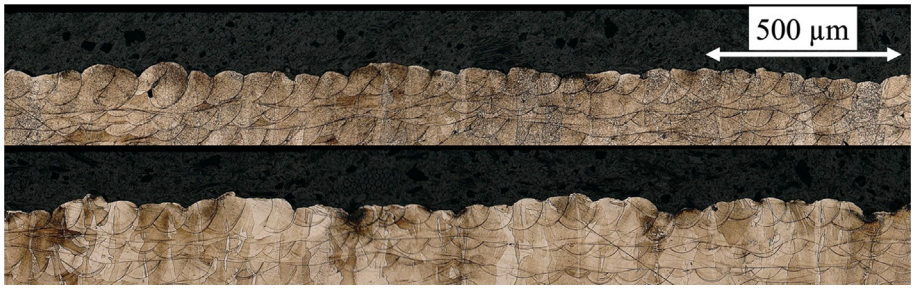

Fig. 11. Exemplary sections of the images where the solidified melt pool width and depth was measured. The top image depicting P1.1, the bottom P1.2.

Table 2
Melt pool dimensions for P1.1 and P1.2, the first and last ten vectors are neglected.

#	Melt pool width [µm]		Melt pool depth [µm]	
	Average	Std Dev	Average	Std Dev
1.1	131	20	70	16
1.2	111	14	61	14

The increase in melt pool width for P1.1 compared to P1.2 is in conjunction with the respective skewness of the laser beam. To verify whether an expanded beam actually results in the observed signal decrease, or whether the signal decrease originates from the tilted measurement, P10.2 is examined. It provides data from the process where the diameter of the perpendicular beam is expanded without changing any other parameter. Indeed, Fig. 12 provides proof that with an expanded beam (which inherently results in lower intensities) proportionally lower acoustic and IR emissions are the consequence. The latter is also evident from the OT data, where the scatter between consecutive layers increases when defocusing. To rule out an additional measurement error, the homogeneity of the camera's sensitivity was investigated using the same heat source which was already applied in Section 2.3 for the pyrometer's calibration. It was placed in the area of group 1 and 2, and several measurements were performed. They showed a consistency with average discrepancy below 1%. This can be interpreted as the camera's sensitivity being homogeneous in the relevant area. This deems the two optical sensors capable of detecting laser defocusing and the potential errors associated to it and a fortiori rules out an overlaying optical measurement error.

3.2.2. Acoustic signal attenuation theory

Concerning the acoustic signal (dotted line) in Fig. 10 however, the following observation is instantaneously apparent: Sound coming from a source farther away (group 1) is received at a much lower sound pressure level p which cannot only be attributed to the deflected beam described above. This is primarily due to the half-spherical propagation of sound originating from the melt pool (inverse distance law), which results in a scaling of the pressure reciprocally to the radius $p(r) \propto 1/r$. This holds true for free field acoustics. However, since some reverberation was detected in Section 3.1 for frequencies below 100 kHz, this decay is counteracted, and the hereby given analytical result is not directly applicable.

Aside from the distribution of the energy across an ever-growing area, there is another factor at play reducing the received signal with travelled distance: damping. Atmospheric absorption α [dB/m] is well described by Bass et al. [64,65] for still air under standard climatic conditions, by the following equation:

$$\alpha = \frac{20f^2}{\ln(10)}\left[\left(\frac{1.84\cdot 10^{-11}}{\left(\frac{T_0}{T}\right)^{1/2}\frac{p}{p_0}}\right) + \left(\frac{T_0}{T}\right)^{5/2} \times \left(0.1068\frac{e^{-3352/T}f_{r,N}}{f^2+f_{r,N}^2} + 0.01278\frac{e^{-2239.1/T}f_{r,O}}{f^2+f_{r,O}^2}\right)\right]$$

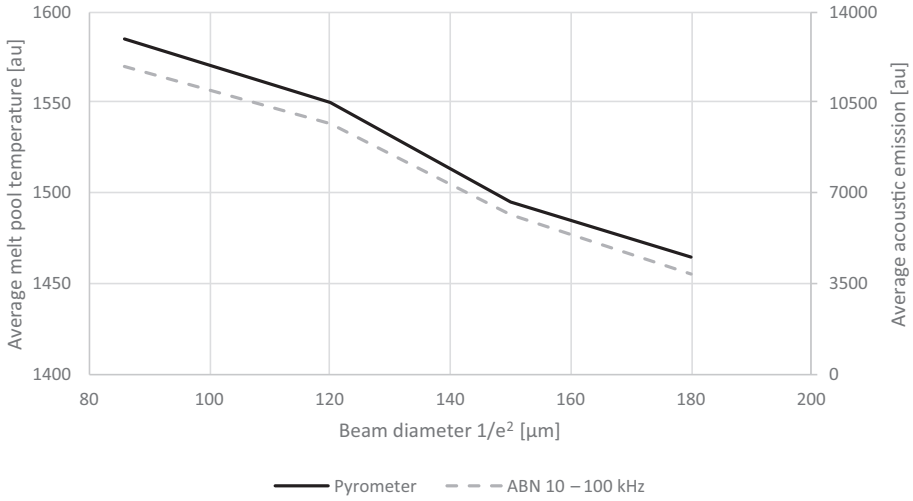

Fig. 12. ABN and temperature signal both decrease with expanding beam diameter. Signal from P10.2 where the beam is expanded deliberately.

The resulting damping is not only scaled by distance, but also a function of frequency f [Hz]. Where higher frequencies are subject to more intense damping. The transporting media's pressure p [atm] and temperature T [K], as well as its composition (especially humidity) also play a role. They are taken into account using the relaxation frequency of the two major components of air: nitrogen $f_{r,N}$ and oxygen $f_{r,O}$. Empirical equations describing those two entities, depending on temperature, pressure and humidity, are given by Bass et al. and are not covered in detail here.

The conditions within the process chamber, however, do not resemble the ones for which the above equation necessarily holds true, since there is an intentional absence of oxygen in the shielding gas. The equation is therefore adjusted by neglecting the term covering the oxygen's relaxation frequencies and accordingly scaling the nitrogen's part. Since ideal gas conditions can be assumed, the simplified equation is the following:

$$\alpha = \frac{20f^2}{\ln(10)}\left[\left(\frac{1.84\cdot 10^{-11}}{\left(\frac{T_0}{T}\right)^{1/2}\frac{p}{p_0}}\right)+\left(\frac{T_0}{T}\right)^{5/2}\left(0.1068\,\frac{e^{-3352/T}f_{r,N}}{f^2+f_{r,N}^2}\right)\right]$$

According to Knudsen [66], N_2 has an absorption coefficient in the same order of magnitude as dry air; at least up to a maximum frequency of 10 kHz, up to which he was able to verify. Hence it is admissible to compare the original equation with humidity set to 0 to the simplified equation for verification. The results demonstrate an almost constant difference of 0.0014 dB, a difference which still lacks in significance beyond 700 kHz.

Further findings by Knudsen are, that the presence of humidity in a nitrogen environment is almost irrelevant for the absorption coefficient, therefore the lack of a moisture measurement for the herein conducted experiment is nullified and assuming zero humidity is justified, especially considering that the build chamber is regularly flushed with dry nitrogen. Knudsen furthermore states that major absorption in air is attributed to an interaction between the H_2O and O_2 molecules. This can be confirmed when inspecting the significance of the water vapour concentration factor in the two relaxation frequencies $f_{r,N}$ and f_O provided by Bass et al. With this knowledge, the oxygen content of the above equation can safely be omitted entirely, although the real concentration was maintained only below 0.15%. All of this further substantiates the above taken measures to simplify the equation.

Fig. 13 shows a plot of the two discussed phenomena (distribution and damping) combined for several frequencies and neglecting reverberation. The line for 1 kHz mainly represents the distribution effects, since the share of damping remains negligible up to a frequency of 16 kHz, where it still accounts for slightly less than 1% of the total loss.

Three messages follow from the graph and the analysis: First, the acoustic signal mainly decays inverse proportionally to the distance, rendering the sensor placement an important task. Due to its limited amplitude, reverberation does not play a crucial role in mitigating this decay. Second, frequency dependent damping is practically irrelevant below 16 kHz for the given circumstances but plays a major role above 100 kHz with the present distances. And third, some potential deviation (+/− 5 K or +/− 10 mbar) from the presented process conditions apparently has no noteworthy impact (max deviation 0.3 dB/m) on the analysis above, rendering the results stable and thus (after verification) industrially applicable for compensation.

Due to this distribution and damping, frequencies beyond 300 kHz are not received from group 1 (distance 250–320 mm). Any future investigation on higher frequencies will be carried out using group 2 samples.

Section 3.1 demonstrated the presence of reverberation below 100 kHz in the given chamber. However, since the reverberation is on a low level, the analytical results presented here are nevertheless applied for compensation. The solid lines in Fig. 10 represent such compensated values. And by that amplify a second observation: A declining trend for the signal in group 2, which is already present in group 1 and extremely subtle also in the optical measurements from group 2. The skewness of the beam cannot be hold accountable for this anomaly, since the samples of group 2 are symmetrically arranged around the scanner's origin (see Fig. 1). Shielding gas fluctuations could be responsible for this instead, since the overall trend decreases towards the shielding gas nozzle. In fact, a corresponding linear trend is present in the shielding gas speed across the build plate, with minimal speed of 2.6 m/s at the outlet and a maximum of 3.0 m/s on the inlet side. An additional reason for this trend can be found in the angle under which the sound approaches the microphone. According to Preisser et al. [67], the present etalon demonstrates a certain directional response at least in water. The difference in media (water versus nitrogen) plus the fact that the studies at hand were carried out using a protection kit, prevent the direct application of the results of Preisser et al. The given reasons need further investigation and solid proof, which is beyond the scope of this work. Anyhow, metallographic images of the involved samples do not highlight any corresponding trend in the resulting material quality. Thus, it

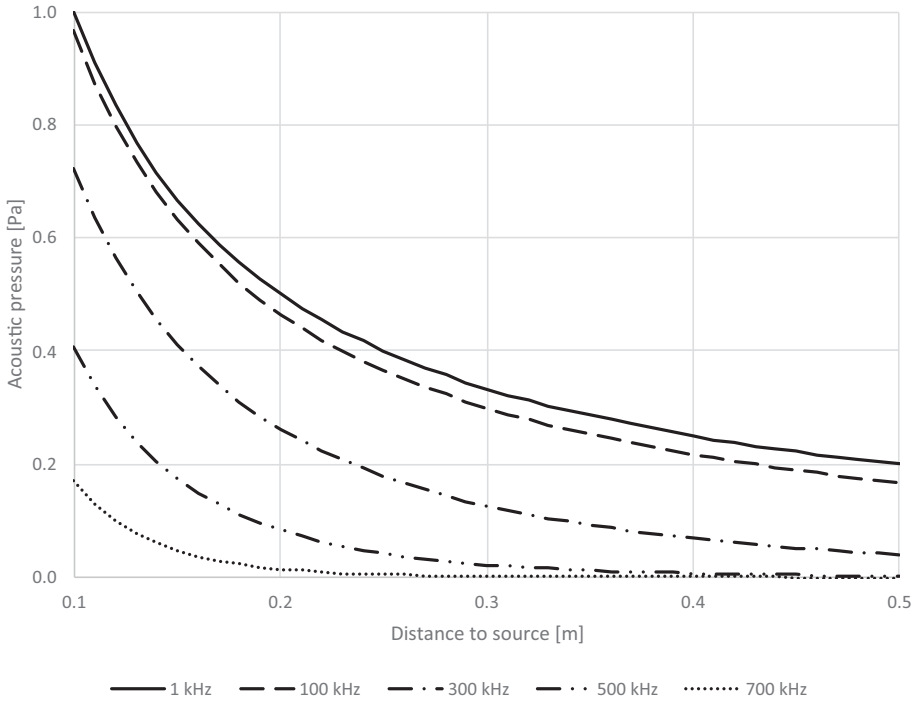

Fig. 13. Plot of acoustic pressure decrease over relevant distance range (for LPBF systems of comparable size) due to intensity distribution and atmospheric damping for different frequencies in a free field. Assuming an ideal point source with 1 Pa sound pressure at 0.1 m distance for 1 Hz, and uniform intensity distribution across all frequencies at the source.

needs to be assumed, that the relevance of this regarding the parts is negligible. Since this trend is position dependent, it can be counteracted by appending an additional term to the compensation derived above.

3.2.3. Results on sensing distance and angle susceptibility

It can be summarized that there exists a distance and angle dependent signal attenuation which affects the ABN, especially critical for frequencies above 300 kHz. Basic means for compensation are presented. According to this study, no such limitations were detected on the optical instruments. Furthermore, two position dependent process deviations were exposed as a by-product. First, the impact of a tilted laser beam on the melt pool temperature and acoustic emissions are discussed. And second, a trend in the shielding gas flow quality was uncovered. While the microphone exhibited a sensitivity regarding this trend of 15% for the frequency band of 10–100 kHz (measured between P5.2 and P12.2, see Fig. 10), the pyrometer is deemed less sensitive with a sensitivity for the same scenario of only 1% and the OT is practically insensitive to it with only 0.4% change in signal intensity.

3.3. Directional sensitivity

A sensor's potential susceptibility to different scan directions is difficult to differentiate from process related discontinuities originating from those scan directions, especially when the sensor integration is rigid, or the process circumstances are anisotropic to begin with (e.g. fixed shielding gas direction). With the microphone being free to be positioned throughout the machine volume, a fundamental evaluation is established on the acoustic signal. The hereby acquired data is additionally used to affirm the overall sensitivity benchmark established in the previous section.

3.3.1. Shielding gas interaction

By detailed examination of the acoustic signal for different hatchings, a pattern emerges on every other layer throughout the whole build, an example can be found in Fig. 14. While the acoustic signature of layer 42 exhibits a hair-comb pattern, layer 43 of the same part is more constant in amplitude on the time scale throughout the whole bandwidth.

This can be explained with the global orientation of the hatching. The bi-directional pattern is rotated by 90° every layer, see Fig. 1 or Fig. 3, where the hatching of two subsequent layers is depicted. The angle of 90° is chosen to allow for easier metallographic analysis of the resulting melt tracks, since they align parallel to the edge of the cube. As a result, the melt pool moving direction either aligns perpendicular to the shielding gas direction or parallel (see Fig. 1 again). For the orthogonal orientation, the moving direction (left–right versus right-left) apparently does not have a significant influence on the signal (see Fig. 14, right), which is plausible. When scanning parallel to the shielding gas stream however (back versus forth), it apparently plays a crucial role whether the scanning direction is with or against the gas direction. The former is expected to be compromised by the increased interaction with soot, since the relative speed between laser and trail of soot is decreased. A second reason could also be the orientation of the microphone with regards to the melt pool (directional sensitivity). To further investigate this theory, scans with the same parameters but without powder (less noise) were performed on a bare build plate. The microphone was then placed in the original position (upstream), as well as to the side and downstream of the process, all while still maintaining the same distance and orientation to the process (see the alternative positions in Fig. 1). No significant difference regarding the pattern could be extracted, leaving the microphone-melt pool orientation dependency negligible and the source of the observed pattern a real process deviation: The laser beam interacting with the soot.

3.3.2. Quantitative analysis of the shielding gas interaction

For simplified data analysis, the following quantitative comparison neglects the jumps between vectors and the related laser-on and -off effects with their characteristic spikes in signal, and hence

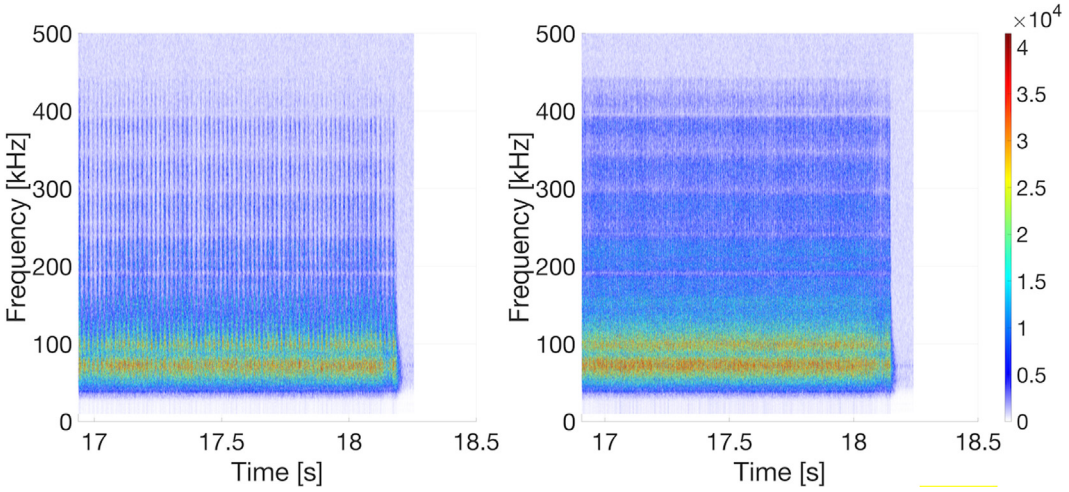

Fig. 14. ABN of P1.2 from layer 42 (left) and 43 (right). Even numbered layers are scanned parallel to the shielding gas direction, odd numbered layers are scanned perpendicular.

leaves the bare readings from the core of each vector. More precisely, 550 μs around each local minimum (jump) are neglected. Additionally, the first and last ten vectors of each layer are neglected as well to exclude boundary effects. Fig. 15 quantifies the content of Fig. 14 and can be condensed to two statements:

First, the overall acoustic emissivity is indeed much lower for scanning parallel (−32%) to the gas stream compared to orthogonal. The aforementioned soot which reduces the laser input—and by that affecting the melt pool temperature and thus reducing acoustic emissions—could be hold accountable for this.

The second remark about Fig. 15 is regarding the difference of results between successive vectors. Which is larger for the parallel case by a factor of 2.6. The reason for this can again be found in the soot trail: Since the parallel scanning combines the best- and worst-case scenario—scanning against and with the shielding gas—the large difference in amplitude between the two is plausible.

3.3.3. Detection of shielding gas interaction by the pyrometer

This behaviour is also observed by the pyrometer, although less notable. The vectors' temperature values $T_{i,j}$ are compressed into two numbers for each vector j: namely the mean temperature $\mu_{T,j}$ and the associated standard deviation $\sigma_{T,j}$. Those numbers of the vectors constituting layers 42 (parallel) and 43 (orthogonal) under investigation here, are compared twofold:

Firstly, the mean values $\mu_{T,j} \forall j \in [10..130]$ are plotted (see Fig. 16). They show the same pattern as their acoustic counterpart, however, on a less sensitive level. Overall, there is only 2% decrease from orthogonal to parallel (compared to −32% for the acoustic case, the same sensitivity difference as demonstrated in Section 3.2).

The resemblance is also retrieved from the standard deviation $\sigma_{T,j}$ (not plotted): The parallel scanning exhibits a 17% increase in standard deviation compared to the steadier orthogonal scanning.

The two findings are congruent with the results from the microphone while showing a limited sensitivity.

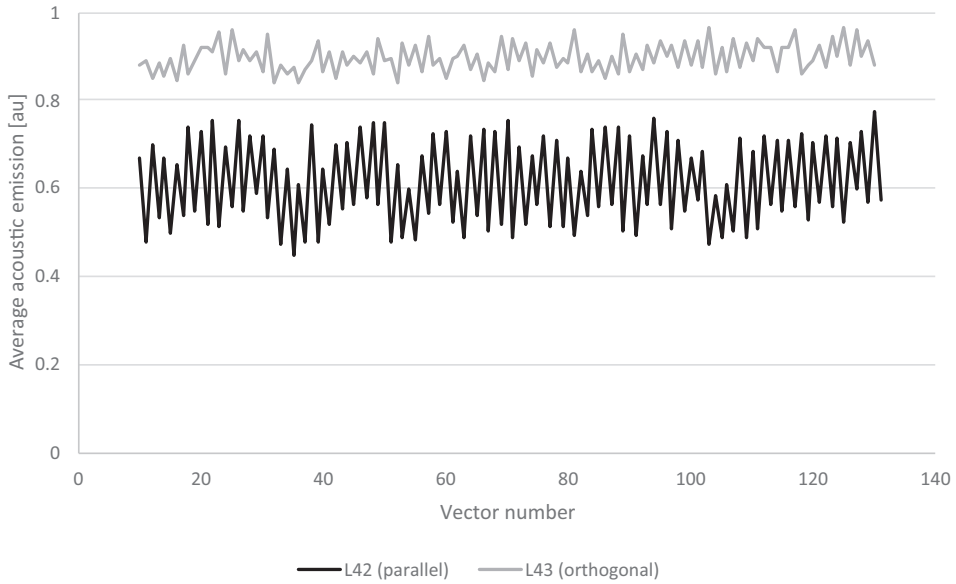

Fig. 15. Mean acoustic emission for each vector of layer 42 and 43 from P1.2. The first and last ten vectors are neglected.

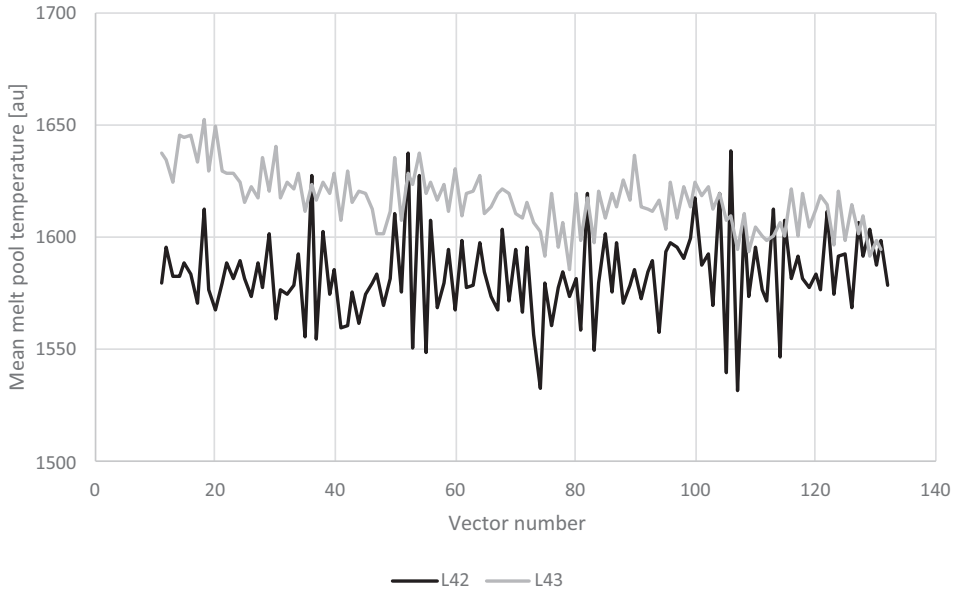

Fig. 16. Mean vector temperature values of layers 42 (parallel) and 43 (orthogonal) of P1.2, the first and last ten vectors are neglected.

3.3.4. Detection of shielding gas interaction through OT

The off-axis camera is also able to detect this phenomenon. In the region below the scanner (group 2), the average intensity is 4% lower in layers scanned parallel to the shielding gas direction compared to layers scanned orthogonal. For this analysis, the images of layers 34 through 283 from parts P1.2 and P4.2-P12.2 were considered. One manageable reason for this insensitivity lies in the fact, that the exposure settings of the camera are chosen such, that they yield satisfactory results for a variety of process parameters and even different materials. Therefore, for a single material and parameter set, the already limited dynamic range of the camera (8 bit) is usually not fully exploited.

3.3.5. Influence of shielding gas speed on signal scatter

The presented findings first of all confirm that vectors oriented parallel to the shielding gas exhibit a larger discrepancy in mean melt pool temperature. Since the shielding gas stream across the build plate is believed to be the main driver of this observation, it is natural to investigate the impact of the relative speed between melt pool and shielding gas. This is done by additionally inspecting the signal scatter of P7 to P9, which are built using different scan speeds while maintaining a constant energy input. The results are summarized in Table 3 and obtained through each sample's overall signal imbalance $\sigma_{v,d}$. Which for a given sample with speed v (0.6, 1.2, 2.4 and 4.8 m/s) and direction d (parallel and orthogonal) is determined by the following equation:

$$\sigma_{v,d} = \frac{1}{\bar{\sigma_T}} \sqrt{\frac{\sum_{j=10}^{130} \left(\sigma_{T,j} - \bar{\sigma_T}\right)^2}{120}}$$

where $\sigma_{T,j}$ is the standard deviation of a vector j's temperature. $\bar{\sigma_T}$ denotes the average of the standard deviation of the $n = 120$ vectors involved. Thus, the above equation basically presents the standard deviation of the individual vectors' standard deviations, and hence represents how the vectors' signal scatter level changes between individual vectors.

The results clearly indicate two findings: First, the shielding gas parallel bi-directional scanning always yields a higher signal scatter compared to orthogonal scanning, which is considered negative in general, since it indicates consecutive vectors with larger difference in process conditions. Second, the discrepancy between parallel and orthogonal is indeed maximum for the case which is the closest to the shielding gas stream velocity.

The investigations unveil two additional results regarding the sensors: First, the pyrometer with its 12.5 kHz sampling frequency is found unsuitable for providing reliable data at scan speeds of 4.8 m/s. Second, the thermography camera can be considered practically insensitive regarding the phenomenon of shielding gas influenced melt pool dynamics. Considering the unimportance of the effect, the pyrometer is reasonably sensitive, while the microphone is most sensitive.

3.3.6. Results on sensor sensitivity

To conclude the actual scan-direction investigation, the relative material density of the involved samples is determined using metallographic images for pore detection. The density of samples P1.2, P7.2 and P8.2 is 99.8% or higher. Only P9.2, the candidate with the highest scan speed, exhibited a density of only 97.9%. This is not surprising, since the speed was deliberately chosen to cause unstable processing conditions. To further investigate the impact of

Table 3
Sensor signal scatter between successive vectors as a result of scanning parallel or orthogonal to the shielding gas (~2.8 m/s). Lower is better, results are normalized sensor-wise for comparability.

Scan speed	ABN		Pyrometer		OT	
[m/s]	Parallel	Orthogonal	Parallel	Orthogonal	Parallel	Orthogonal
0.6	0.5	0.3	0.6	0.5	0.8	0.9
1.2	0.7	0.2	0.6	0.4	0.7	0.7
2.4	1.0	0.1	1.0	0.4	0.7	0.7
4.8	0.4	0.2	–	–	1.0	1.0

shielding gas parallel scanning on material density, P2.2 is considered. This specimen is built with shielding gas parallel bi-directional scanning only (no 90° rotation between layers). Its density is just as high as the reference specimen. All measurements were verified using Archimedes' principle for density determination. The data found leads to the following conclusions: While allowing to exclude directional sensitivity for all of the involved sensors as a sensor related measurement issue, this investigation uncovered a real process deviation incidentally: Scanning in shielding gas direction results in more process scatter. Material density-wise however, when only scanning in shielding gas direction every other vector (bi-directional), no negative impact was determined. Nevertheless, unnecessary shielding gas synchronous scanning should be omitted, since the increased signal scatter reduces readability and by that might conceal other process phenomena in the monitoring data.

3.4. Detecting interlayer defects

Two process phenomena (spatter as a result of overhang and defocusing which results in lack of fusion) have been exploited in the previous sections to compare the sensors' general ability to deal with changing measuring conditions. This investigation serves to affirm the quantitative findings of previous sections. Therefore, in P3, a flawed layer is deliberately triggered in three instances by creating horizontal voids through omitting several layers from scanning (see Fig. 18). The first subsequent layer which again contains all vectors practically faces an unnaturally deep powder bed, as it would result from a recoater defect or short-feed of powder. Scanning this results in a horizontal collection of voids. A detailed investigation on this topic was carried out by du Plessis et al. [68,69].

The gap heights were set to 120 μm, 300 μm and 480 μm. The results of Fig. 17 lead to the following verdict: The initial gap was low enough for the laser to melt through the whole stack without creating any persisting lack of fusion. This happened unnoticed by the OT camera, while both pyrometer and microphone show a signal reduction (see Table 4). On the contrary, the third gap was extreme: The layer 317, which was basically welded into loose powder, did not sufficiently attach to the fins on either side. This is evident from the OT image of the first layer after the gap (see Fig. 18) and was visible during the process with the naked eye. Moreover, this undefined process state resulted in one of the pyrometer's two channels exceeding an upper or lower bound, which results in the retention of any further values for as long as this condition persists. As this was the case with the investigated layers for more than 30% of the measurements, it renders the given values useless. After some layers, the geometrical integrity was restored, and the process returned to normal conditions.

According to Table 4, both the microphone as well as the pyrometer response to this underlying inhomogeneity with a similar signal reduction. The OT camera is less sensitive for the small gap heights, the 480 μm gap however is received more intense.

4. Conclusion

In this study, the comparison of a microphone, an on-axis two-colour pyrometer and an off-axis thermography camera was performed on an LPBF laboratory machine under process conditions. The sensors were tried for three domains of fundamental measurement challenges: temporal resolution, impact of different sensing

Fig. 17. On the left, P3 with three gaps causing layered defects. On the right, metallography of the specimen P3.2. The dashed region indicates the area of the smallest gap.

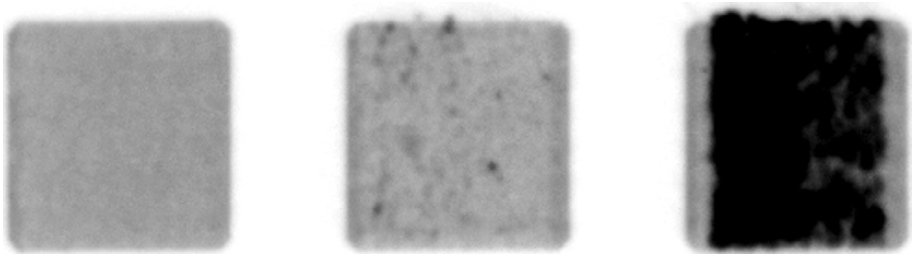

Fig. 18. OT images of the first layer after each void. Left, L171 (unimpeded process), middle L244 some hotspots and spatter visible, and right L317 containing a large hotspot in the area of loose powder as well as some spatter due to the layer not attaching to the fins on the side.

Table 4
Results from the gap scans in P3.2. Reference is taken from L77 where no gap was present, to which all results are sensor-individually normalized. ABN covers 100 – 700 kHz. Results in brackets indicate invalid measurement conditions.

Scenario	Layer	ABN [%]	Pyrometer [%]	OT [%]
Reference	77	100	100	100
120 μm gap	1st subsequent layer	93	95	100
120 μm gap	2nd subsequent layer	95	96	101
300 μm gap	1st subsequent layer	78	83	99
300 μm gap	2nd subsequent layer	88	88	95
480 μm gap	1st subsequent layer	75	(116)	255
480 μm gap	2nd subsequent layer	91	(97)	137

distances and location, and different scanning directions and speeds. Moreover, process deviations in form of interlayer flaws, lack-of-fusion, defocusing and spatter are recorded.

With a sampling frequency of 12.5 kHz, the pyrometer exhibits the necessary temporal resolution for sub-vector phenomena to be observable, provided scan speeds are below 4.8 m/s. The extremely high temporal resolution of the microphone was found to be mainly applicable in higher frequencies, as reverberation happening within the build chamber causes smearing of the results below 100 kHz. Nevertheless, short-lived phenomena in the millisecond scope were detected, especially in the higher frequency bands, which provides justification for such a high-bandwidth microphone. The camera does not provide a temporal resolution, still, it was able to capture spatter at almost the same level of detail as its two counterparts. Furthermore, by its spatial resolution, it is the only sensor capable of recording the extent and direction of spatter deposition. With its two-colour design, the pyrometer is able to compensate for changes in spot fill factor and angle of incidence, arising from working in different areas of the scan field and thus with a deflected beam. Similar results are obtained for the camera. The acoustic signal on the contrary demonstrates distance dependent sensitivity and potentially also an angular response. The melt pool moving direction relative to the sensor does not trigger different sensitivities on any of the reviewed sensors. Overall, the sensitivity regarding any process deviation is the highest with the microphone. The pyrometer and the camera are less sensitive by a factor of up to 15 and 40, respectively.

Aside from the sensor performance, the study at hand unveiled the following general LPBF findings: The pyrometer and the microphone received a reduced, instead of an increased signal as a result of scanning an overhang area. This can be the result of a melt pool enlargement and needs further investigation. Scanning parallel and in the same direction as the shielding gas imposes up to double the amount of scatter on the measurement and therefore conceals other process anomalies. This is most prominent if the scan speed and shielding gas velocity are equal. Deflection of the laser beam to reach the corner of the scan field results in a reduced signal emission (acoustic and electromagnetic) and a wider melt track in the material. The acoustic and IR emission is inverse proportional to the beam diameter.

From the findings above, the following sensor specific recommendations are projected: For melt pool intensity recording, a two-colour pyrometer appears to be a promising and robust candidate. Aside from the Q-temperature, the single channel temperatures should be recorded likewise, in order to obtain more information about the melt pool and potential measurement errors resulting from signal saturation. The microphone appears to be interesting for independent signal validation and general process development. In order for it to provide more straight forward data however, the most equidistant location to the powder bed needs to be selected for the sensor head. For future studies on the given system, it will be mounted at the ceiling of the chamber near the laser window. Additionally, analytical compensation approaches are provided to compensate for the remaining distance dependent attenuation. Additional terms for the sensor's angular response are to be determined, and their application related scaling needs to be specified. The pencil-lead-break-test was found helpful in providing a reliable and broad band impulse sound source for such undertakings inside a machine. The thermography camera is a simple, robust and inexpensive device. In this study, it did provide additional insights by recording the amount and landing area of spatter, additionally it helped in verifying the signals of the other sensors. To increase its mediocre sensitivity, process parameter specific exposure settings should be considered to exploit its whole dynamic range. Additionally, a higher resolution can avoid smoothing and thus hiding of local effects.

Data availability

The raw data required to reproduce these findings cannot be shared at this time as the data also forms part of an ongoing study. The processed data required to reproduce these findings are available to download from http://dx.https://doi.org/10.17632/v3ys96h6jc.1.

CRediT authorship contribution statement

Kai Gutknecht: Writing – original draft, Data curation, Formal analysis, Validation, Software, Methodology, Investigation, Conceptualization, Visualization, Writing – review & editing. **Michael Cloots:** Conceptualization, Project administration. **Ryan Sommerhuber:** Validation, Writing – review & editing. **Konrad Wegener:** Conceptualization, Project administration, Supervision, Validation, Writing – review & editing.

Declaration of Competing Interest

The authors declare that they have no known competing financial interests or personal relationships that could have appeared to influence the work reported in this paper.

Acknowledgement

This research did not receive any specific grant from funding agencies in the public, commercial, or not-for-profit sectors.

Appendix

See Table 5.

Table 5
Optical and acoustic conditions for the specimens' placement in the build envelope.

#	Laser angle of incidence [deg]	Laser diameter aspect ratio [%]	Distance to microphone [mm]	Acoustic delay [ms]
1.1	21	107	319.8	0.914
2.1	20	106	304.9	0.871
3.1	18	105	290.5	0.830
4.1	20	107	305.1	0.872
5.1	19	106	289.7	0.828
6.1	17	105	275.0	0.786
7.1	19	106	291.1	0.832
8.1	18	105	275.2	0.786
9.1	16	104	260.0	0.743
10.1	19	106	277.7	0.793
11.1	17	105	261.5	0.747
12.1	15	104	245.8	0.702
1.2	4	100	165.4	0.473
2.2	3	100	160.9	0.460
3.2	3	100	158.8	0.454
4.2	2	100	150.1	0.429
5.2	1	100	145.7	0.416
6.2	2	100	144.2	0.412
7.2	2	100	135.9	0.388
8.2	1	100	131.9	0.377
9.2	2	100	130.9	0.374
10.2	3	100	123.5	0.353
11.2	2	100	119.8	0.342
12.2	3	100	119.6	0.342

References

[1] T. Wohlers, T. Caffrey, I. Campbell, Wohlers Report (2016) 2016.
[2] AM Special Interest Group, Shaping our National Competency in Additive Manufacturing, 2012.
[3] NIST, Measurement science roadmap for metal-based additive manufacturing, Energetics Incorporated (2013), https://doi.org/10.1007/s13398-014-0173-7.2.
[4] T. Kolb, P. Gebhardt, O. Schmidt, J. Tremel, M. Schmidt, Melt pool monitoring for laser beam melting of metals: Assistance for material qualification for the stainless steel 1.4057, Procedia CIRP. 74 (2018) 116–121, https://doi.org/10.1016/j.procir.2018.08.058.
[5] T. Kolb, R. Elahi, J. Seeger, M. Soris, C. Scheitler, O. Hentschel, J. Tremel, M. Schmidt, Camera signal dependencies within coaxial melt pool monitoring in laser powder bed fusion, Rapid Prototyping J. 26 (1) (2020) 100–106, https://doi.org/10.1108/RPJ-01-2019-0022.
[6] S.K. Everton, M. Hirsch, P. Stravroulakis, R.K. Leach, A.T. Clare, Review of in-situ process monitoring and in-situ metrology for metal additive manufacturing, Mater. Des. 95 (2016) 431–445, https://doi.org/10.1016/j.matdes.2016.01.099.
[7] T.G. Spears, S.A. Gold, In-process sensing in selective laser melting (SLM) additive manufacturing, Integrating Mater. Manuf. Innovation 5 (1) (2016) 16–40, https://doi.org/10.1186/s40192-016-0045-4.
[8] T. Craeghs, S. Clijsters, J.-P. Kruth, F. Bechmann, M.C. Ebert, Detection of process failures in layerwise laser melting with optical process monitoring, Phys. Procedia 39 (2012) 753–759, https://doi.org/10.1016/j.phpro.2012.10.097.
[9] I.A. Okaro, S. Jayasinghe, C. Sutcliffe, K. Black, Automatic fault detection for selective laser melting using semi-supervised machine learning, (2018) 1–35. DOI: 10.20944/preprints201809.0346.v1
[10] A.G. Demir, C. De Giorgi, B. Previtali, Design and implementation of a multisensor coaxial monitoring system with correction strategies for selective laser melting of a maraging steel, J. Manuf. Sci. Eng., Trans. ASME 140 (2018), https://doi.org/10.1115/1.4038568.
[11] T. Kolb, L. Müller, J. Tremel, M. Schmidt, Melt pool monitoring for laser beam melting of metals: Inline-evaluation and remelting of surfaces, Procedia CIRP. 74 (2018) 111–115, https://doi.org/10.1016/j.procir.2018.08.052.
[12] M. Pacher, L. Mazzoleni, L. Caprio, A.G. Demir, B. Previtali, Estimation of melt pool size by complementary use of external illumination and process emission in coaxial monitoring of selective laser melting, J. Laser Appl. 31 (2) (2019) 022305, https://doi.org/10.2351/1.5096117.
[13] G. Dursun, B. Pehlivanogullari, C. Sen, A. Orhangul, An investigation upon overhang zones by using finite element modelling and in-situ monitoring systems, Procedia CIRP. 93 (2020) 1253–1258, https://doi.org/10.1016/j.procir.2020.04.118.
[14] M. Doubenskaia, M. Pavlov, Y. Chivel, Optical system for on-line monitoring and temperature control in selective laser melting technology, Key Eng. Mater. 437 (2010) 458–461, https://doi.org/10.4028/www.scientific.net/KEM.437.458.
[15] Y. Chivel, I. Smurov, Temperature monitoring and overhang layers problem, Phys. Procedia 12 (2011) 691–696, https://doi.org/10.1016/j.phpro.2011.03.086.
[16] U. Thombansen, A. Gatej, M. Pereira, Process observation in fiber laser-based selective laser melting, Opt. Eng. 54 (1) (2015) 011008, https://doi.org/10.1117/1.OE.54.1.011008.
[17] A. Slaughter, M. Yampolskiy, M. Matthews, W.E. King, G. Guss, Y. Elovici, How to ensure bad quality in metal additive manufacturing: In-situ infrared thermography from the security perspective, ACM Int. Conf. Proc. Ser. Part F1305 (2017), https://doi.org/10.1145/3098954.3107011.
[18] Y. Hagedorn, F. Pastors, Process monitoring of laser beam melting, Laser Tech. J. 15 (2) (2018) 54–57, https://doi.org/10.1002/latj.v15.210.1002/latj.201800009.
[19] P.A. Hooper, Melt pool temperature and cooling rates in laser powder bed fusion, Addit. Manuf. 22 (2018) 548–559, https://doi.org/10.1016/j.addma.2018.05.032.
[20] V. Renken, L. Lübbert, H. Blom, A. Von Freyberg, A. Fischer, Model assisted closed-loop control strategy for selective laser melting, Procedia CIRP, Elsevier B.V. (2018) 659–663, https://doi.org/10.1016/j.procir.2018.08.053.
[21] V. Renken, A. von Freyberg, K. Schünemann, F. Pastors, A. Fischer, In-process closed-loop control for stabilising the melt pool temperature in selective laser melting, Prog. Additive Manuf. 4 (4) (2019) 411–421, https://doi.org/10.1007/s40964-019-00083-9.
[22] W. Zouhri, J.Y. Dantan, B. Häfner, N. Eschner, L. Homri, G. Lanza, O. Theile, M. Schäfer, Optical process monitoring for Laser-Powder Bed Fusion (L-PBF), CIRP J. Manuf. Sci. Technol. 31 (2020) 607–617, https://doi.org/10.1016/j.cirpj.2020.09.001.
[23] J.-B. Forien, N.P. Calta, P.J. DePond, G.M. Guss, T.T. Roehling, M.J. Matthews, Detecting keyhole pore defects and monitoring process signatures during laser powder bed fusion: A correlation between in situ pyrometry and ex situ X-ray radiography, Addit. Manuf. 35 (2020) 101336, https://doi.org/10.1016/j.addma.2020.101336.
[24] B. Yuan, B. Giera, G.M. Guss, M.J. Matthews, S. McMains, Semi-supervised convolutional neural networks for in-situ video monitoring of selective laser melting, in: Proceedings - 2019 IEEE Winter Conference on Applications of Computer Vision, WACV 2019, Institute of Electrical and Electronics Engineers Inc., 2019. DOI: 10.1109/WACV.2019.00084.
[25] S. Clijsters, T. Craeghs, S. Buls, K. Kempen, J.-P. Kruth, In situ quality control of the selective laser melting process using a high-speed, real-time melt pool monitoring system, Int. J. Adv. Manuf. Technol. 75 (5-8) (2014) 1089–1101, https://doi.org/10.1007/s00170-014-6214-8.
[26] T. Toeppel, P. Schumann, M.C. Ebert, T. Bokkes, K. Funke, M. Werner, F. Zeulner, F. Bechmann, F. Herzog, 3D analysis in laser beam melting based on real-time process monitoring, Materials Science and Technology Conference and Exhibition 2016, MS and T 2016 (1) (2016) 123–132.
[27] B.M. Lane, S. Grantham, H. Yeung, C. Zarobila, J. Fox, Performance characterization of process monitoring sensors on the nist additive manufacturing metrology testbed, Solid Free Fabr Symp (2017) 1279–1288, https://doi.org/10.1007/s10024-004-7084-0.
[28] Z. Yang, Y. Lu, H. Yeung, S. Krishnamurty, Investigation of deep learning for real-time melt pool classification in additive manufacturing, in: IEEE International Conference on Automation Science and Engineering, IEEE, 2019: pp. 640–647. DOI: 10.1109/COASE.2019.8843291

[29] F. Bayle, M. Doubenskaia, Selective laser melting process monitoring with high speed infra-red camera and pyrometer, Proceedings of SPIE. 6985 (2008), https://doi.org/10.1117/12.786940 698505.
[30] S. Moylan, E. Whitenton, B. Lane, J. Slotwinski, Infrared thermography for laser-based powder bed fusion additive manufacturing processes, AIP Conf. Proc. (2014) 1191–1196, https://doi.org/10.1063/1.4864956.
[31] H. Krauss, T. Zeugner, M.F. Zaeh, Layerwise monitoring of the selective laser melting process by thermography, Physics Procedia, Elsevier B.V. 56 (2014) 64–71.
[32] G. Zenzinger, J. Bamberg, A. Ladewig, T. Hess, B. Henkel, W. Satzger, Process monitoring of additive manufacturing by using optical tomography, AIP Conf. Proc. (2015) 164–170, https://doi.org/10.1063/1.4914606.
[33] V. Carl, Monitoring system for the quality assessment in additive manufacturing, AIP Conf. Proc. 1650 (2015) 171–176, https://doi.org/10.1063/1.4914607.
[34] J. Bamberg, G. Zenzinger, A. Ladewig, In-process control of selective laser melting by quantitative optical tomography, in: 19th World Conference on Non-Destructive Testing, 2016, pp. 1–8, https://doi.org/10.2110/palo.2006.p06-040r.
[35] A. Neef, V. Seyda, D. Herzog, C. Emmelmann, M. Schönleber, M. Kogel-Hollacher, Low coherence interferometry in selective laser melting, Phys. Procedia 56 (2014) 82–89, https://doi.org/10.1016/j.phpro.2014.08.100.
[36] J.A. Kanko, A.P. Sibley, J.M. Fraser, In situ morphology-based defect detection of selective laser melting through inline coherent imaging, J. Mater. Process. Technol. 231 (2016) 488–500, https://doi.org/10.1016/j.jmatprotec.2015.12.024.
[37] V. Renken, S. Albinger, G. Goch, A. Neef, C. Emmelmann, Development of an adaptive, self-learning control concept for an additive manufacturing process, CIRP J. Manuf. Sci. Technol. 19 (2017) 57–61, https://doi.org/10.1016/j.cirpj.2017.05.002.
[38] D. Clark, S.D. Sharples, D.C. Wright, Development of online inspection for additive manufacturing products, Insight: Non-Destructive Testing and Condition Monitoring 53 (11) (2011) 610–613, https://doi.org/10.1784/insi.2011.53.11.610.
[39] H. Rieder, M. Spies, J. Bamberg, B. Henkel, On- and offline ultrasonic characterization of components built by SLM additive manufacturing, AIP Conf. Proc. (2016), https://doi.org/10.1063/1.4940605.
[40] P. Vigneashwara, R. Drissi-Daoudi, S. Shevchik, G. Masinelli, R. Logé, K. Wasmer, Analysis of time, frequency and time-frequency domain features from acoustic emissions during Laser Powder-Bed fusion process, in: Procedia CIRP, Elsevier B.V., 2020: pp. 392–397. DOI: 10.1016/j.procir.2020.09.152.
[41] M.S. Hossain, H. Taheri, In situ process monitoring for additive manufacturing through acoustic techniques, J. Mater. Eng. Perform. 29 (10) (2020) 6249–6262, https://doi.org/10.1007/s11665-020-05125-w.
[42] C. Prieto, R. Fernandez, C. Gonzalez, M. Diez, J. Arias, R. Sommerhuber, F. Lücking, In situ process monitoring by optical microphone for crack detection in Laser Metal Deposition applications, in: 11th CIRP Conference on Photonic Technologies [LANE 2020], 2020.
[43] R.J. Smith, M. Hirsch, R. Patel, W. Li, A.T. Clare, S.D. Sharples, Spatially resolved acoustic spectroscopy for selective laser melting, J. Mater. Process. Technol. 236 (2016) 93–102, https://doi.org/10.1016/j.jmatprotec.2016.05.005.
[44] D. Ye, Y. Zhang, K. Zhu, G.S. Hong, J. Ying, Characterization of acoustic signals during a direct metal laser sintering process, Adv. Energy Sci. Equipment Eng. II (2017) 1315–1320, https://doi.org/10.1201/9781315116174-89.
[45] D. Kouprianoff, N. Luwes, E. Newby, I. Yadroitsava, I. Yadroitsev, On-line monitoring of laser powder bed fusion by acoustic emission: Acoustic emission for inspection of single tracks under different powder layer thickness, in: 2017 Pattern Recognition Association of South Africa and Robotics and Mechatronics (PRASA-RobMech), IEEE, 2017: pp. 203–207.
[46] N. Eschner, L. Weiser, B. Häfner, G. Lanza, Development of an acoustic process monitoring system for selective laser melting (SLM), Solid Freeform Fabrication Symposium (2018) 2097–2117.
[47] Sarah Everton, Phill Dickens, Chris Tuck, Ben Dutton, Using laser ultrasound to detect subsurface defects in metal laser powder bed fusion components, JOM 70 (3) (2018) 378–383, https://doi.org/10.1007/s11837-017-2661-7.
[48] Dongsen Ye, Geok Soon Hong, Yingjie Zhang, Kunpeng Zhu, Jerry Ying Hsi Fuh, Defect detection in selective laser melting technology by acoustic signals with deep belief networks, Int. J. Adv. Manuf. Technol. 96 (5-8) (2018) 2791–2801, https://doi.org/10.1007/s00170-018-1728-0.
[49] S.A. Shevchik, C. Kenel, C. Leinenbach, K. Wasmer, Acoustic emission for in situ quality monitoring in additive manufacturing using spectral convolutional neural networks, Addit. Manuf. 21 (2018) 598–604, https://doi.org/10.1016/j.addma.2017.11.012.
[50] W. Rohringer, T. Heine, R. Sommerhuber, N. Lehmann, B. Fischer, Optical Microphone as Laser-Ultrasound Detector, in: DAGA 2018, München, 2018: pp. 960–963.
[51] B.M. Lane, E.P. Whitenton, S. Moylan, Multiple sensor detection of process phenomena in laser powder bed fusion, Thermosense: Thermal Infrared Applications XXXVIII. 9861 (2016), https://doi.org/10.1117/12.2224390.
[52] .Y Plotnikov, D. Henkel, J. Burdick, K. Bourne, Synchronous multi-sensor monitoring for additive manufacturing, Mater. Eval. 78 (2) (2020) 193–202, https://doi.org/10.32548/2020.me-04073.
[53] Irpd AG, MULTI-BEAM SLM-SYSTEM, (2019). https://cdn.irpd.ch/fileadmin/content_live_2019/www.irpd.ch/00_pic/03_machines/200910_Sales_SLM_systemdescription_UGG.pdf.
[54] F. Wirth, A. Frauchiger, K. Gutknecht, M. Cloots, Influence of the Inert Gas Flow on the Laser Powder Bed Fusion (LPBF) Process, in: International Conference on Additive Manufacturing in Products and Applications, Springer, 2020: pp. 192–204. DOI: DOI: 10.1007/978-3-030-54334-1
[55] M.F Costa Gomes, J.P.M Trusler, The speed of sound in nitrogen at temperatures between T = 250K and T = 350K and at pressures up to 30 MPa, J. Chem. Thermodyn. 30 (5) (1998) 527–534, https://doi.org/10.1006/jcht.1997.0331.
[56] Balthasar Fischer, Wolfgang Rohringer, Nils Panzer, Sebastian Hecker, Acoustic process control for laser material processing, Laser Tech. J. 14 (5) (2017) 21–25, https://doi.org/10.1002/latj.v14.510.1002/latj.201700029.
[57] Marcel Gerstgrasser, Michael Cloots, Josef Stirnimann, Konrad Wegener, Focus shift analysis, to manufacture dense and crack-free SLM-processed CM247LC samples, J. Mater. Process. Technol. 289 (2021) 116948, https://doi.org/10.1016/j.jmatprotec.2020.116948.
[58] K.C. Mills, Recommended values of thermophysical properties for selected commercial alloys, Woodhead Publishing, 2002.
[59] D. Radaj, Wärmewirkungen des Schweissens, 1988.
[60] M. Sause, Investigation of pencil-lead breaks as acoustic emission sources, J. Acoustic Emission 29 (2011) 184–196.
[61] P. Quang-Khang, N. Minh-Dung, K. Matsumoto, I. Shimoyama, ACOUSTIC EMISSION SENSOR USING LIQUID-ON-BEAM STRUCTURE, in: 2015 Transducers-2015 18th International Conference on Solid-State Sensors, Actuators and Microsystems (TRANSDUCERS), IEEE, 2015: pp. 1137–1139
[62] W.C. Sabine, Reverberation, The American Architect 4 (1900).
[63] S. Clijsters, T. Craeghs, J.-P. Kruth, A priori process parameter adjustment for SLM process optimization, Innovative Developments in Virtual and Physical Prototyping - Proceedings of the 5th International Conference on Advanced Research and Rapid Prototyping. (2012) 553–560
[64] H.E. Bass, L.C. Sutherland, L.B. Evans, Atmospheric absorption of sound, J. Acoustical Soc. Am. 51 (1972) 156–157. DOI: DOI: 10.1121/1.1981611.
[65] H.E. Bass, L.C. Sutherland, A.J. Zuckerwar, Atmospheric absorption of sound: Update, J. Acoust. Soc. Am. 88 (1990) 2019–2021. DOI: 10.1121/1.400176.
[66] Vern O. Knudsen, The absorption of sound in air, in oxygen, and in nitrogen—effects of humidity and temperature, J. Acoust. Soc. Am. 5 (2) (1933) 112–121, https://doi.org/10.1121/1.1915638.
[67] Stefan Preisser, Wolfgang Rohringer, Mengyang Liu, Christian Kollmann, Stefan Zotter, Balthasar Fischer, Wolfgang Drexler, All-optical highly sensitive akinetic sensor for ultrasound detection and photoacoustic imaging, Biomed. Opt. Express 7 (10) (2016) 4171, https://doi.org/10.1364/BOE.7.004171.
[68] Anton du Plessis, Stephan Gerhard le Roux, Gerrie Booysen, Johan Els, Directionality of cavities and porosity formation in powder-bed laser additive manufacturing of metal components investigated using X-Ray tomography, 3D Printing and Additive Manuf. 3 (1) (2016) 48–55, https://doi.org/10.1089/3dp.2015.0034.
[69] Anton du Plessis, Ina Yadroitsava, Igor Yadroitsev, Effects of defects on mechanical properties in metal additive manufacturing: A review focusing on X-ray tomography insights, Mater. Des. 187 (2020) 108385, https://doi.org/10.1016/j.matdes.2019.108385.